Egan, Hilary; Ma, Yingjuan; Dong, Chuanfei; Modolo, Ronan; Jarvinen, Riku; Bougher, Stephen; Halekas, Jasper; Brain, David; Mcfadden, James; Connerney, John; Mitchell, David; Jakosky, Bruce

Comparison of Global Martian Plasma Models in the Context of MAVEN Observations

Published in:
Journal of Geophysical Research: Space Physics

DOI:
10.1029/2017JA025068

Published: 01/01/2018

Document Version
Publisher's PDF, also known as Version of record

Please cite the original version:
Egan, H., Ma, Y., Dong, C., Modolo, R., Jarvinen, R., Bougher, S., Halekas, J., Brain, D., Mcfadden, J., Connerney, J., Mitchell, D., & Jakosky, B. (2018). Comparison of Global Martian Plasma Models in the Context of MAVEN Observations. *Journal of Geophysical Research: Space Physics*, *123*(5), 3714-3726. https://doi.org/10.1029/2017JA025068

Journal of Geophysical Research: Space Physics

RESEARCH ARTICLE
10.1029/2017JA025068

Comparison of Global Martian Plasma Models in the Context of MAVEN Observations

Hilary Egan[1], Yingjuan Ma[2], Chuanfei Dong[3], Ronan Modolo[4], Riku Jarvinen[5,6], Stephen Bougher[7], Jasper Halekas[8], David Brain[1,9], James Mcfadden[10], John Connerney[11], David Mitchell[10], and Bruce Jakosky[9]

[1]Astrophysical and Planetary Science, University of Colorado Boulder, Boulder, CO, USA, [2]Department of Earth Planetary and Space Sciences, University of California, Los Angeles, Los Angeles, CA, USA, [3]Department of Astrophysical Sciences and Princeton Plasma Physics Laboratory, Princeton University, Princeton, NJ, USA, [4]LATMOS/IPSL, UVSQ Universite Paris-Saclay, UPMC University Paris CNRS, Guyancourt, France, [5]Finnish Meteorological Institute, Helsinki, Finland, [6]Department of Electronics and Nanoengineering, School of Electrical Engineering, Aalto University, Espoo, Finland, [7]Climate and Space Sciences and Engineering Department, University of Michigan, Ann Arbor, MI, USA, [8]Department of Physics and Astronomy, University of Iowa, Iowa City, IA, USA, [9]Laboratory for Atmospheric and Space Physics, University of Colorado Boulder, Boulder, CO, USA, [10]Space Sciences Laboratory, University of California, Berkeley, Berkeley, CA, USA, [11]NASA/Goddard Space Flight Center, Greenbelt, MD, USA

Key Points:
- Various Martian plasma models show clear morphological differences in the state of the global plasma
- Comparing these models with MAVEN data shows what physics is necessary to model different physical regions
- Modeled escape rates compare well with each other and with estimates from data, despite morphological differences in escaping ion flux maps

Correspondence to:
H. Egan,
hilary.egan@colorado.edu

Citation:
Egan, H., Ma, Y., Dong, C., Modolo, R., Jarvinen, R., Bougher, S., et al. (2018). Comparison of global Martian plasma models in the context of MAVEN observations. *Journal of Geophysical Research: Space Physics*, *123*. https://doi.org/10.1029/2017JA025068

Received 30 NOV 2017
Accepted 10 APR 2018
Accepted article online 19 APR 2018

Abstract Global models of the interaction of the solar wind with the Martian upper atmosphere have proved to be valuable tools for investigating both the escape to space of the Martian atmosphere and the physical processes controlling this complex interaction. The many models currently in use employ different physical assumptions, but it can be difficult to directly compare the effectiveness of the models since they are rarely run for the same input conditions. Here we present the results of a model comparison activity, where five global models (single-fluid MHD, multifluid MHD, multifluid electron pressure MHD, and two hybrid models) were run for identical conditions corresponding to a single orbit of observations from the Mars Atmosphere and Volatile EvolutioN (MAVEN) spacecraft. We find that low-altitude ion densities are very similar across all models and are comparable to MAVEN ion density measurements from periapsis. Plasma boundaries appear generally symmetric in all models and vary only slightly in extent. Despite these similarities there are clear morphological differences in ion behavior in other regions such as the tail and southern hemisphere. These differences are observable in ion escape loss maps and are necessary to understand in order to accurately use models in aiding our understanding of the Martian plasma environment.

1. Introduction

Mars presents a richly complicated and time variable obstacle to the solar wind, consisting of both a conducting ionosphere and localized crustal magnetic fields, but no global dipole field. The interaction region between the undisturbed solar wind and the lower ionosphere hosts a wide variety of physical processes and plays an important role in the energization of planetary particles, atmospheric escape, and upper atmospheric phenomena such as aurora.

Computer models can greatly assist our understanding of these physical processes when used in conjunction with data. The first models of Martian gas dynamics were Spreiter et al. (1970) and Dryer and Heckman (1967). Since then the number of models capable of simulating the Martian magnetosphere has proliferated greatly, and now includes a variety of magnetohydrodynamic (MHD; Dong et al., 2015; Harnett & Winglee, 2007; Ma et al., 2015; Najib et al., 2011; Terada et al., 2009), Hybrid (Boesswetter et al., 2010; Brecht et al., 2016; Holmstrom & Wang, 2015; Jarvinen et al., 2018; Kallio & Janhunen, 2002; Modolo et al., 2016), and test particle (Cravens et al., 2002; Fang et al., 2008; Liemohn et al., 2013) models.

These models have been used to understand an extensive array of Martian plasma processes and interactions. Plasma boundaries (Bertucci et al., 2005; Bößwetter et al., 2004; Najib et al., 2011), spatial ion distribution (Najib et al., 2011), ion escape (Brecht et al., 2016; Brecht & Ledvina, 2014; Dong, Fang et al., 2015; Fang et al., 2010; Kallio, Fedorov et al., 2006), magnetic topology (Liemohn et al., 2006), energetic neutral atoms

(ENAs; Gunell et al., 2006; Kallio, Barabash et al., 2006; Wang et al., 2014, 2016), solar wind alpha particles (Chanteur et al., 2009), and X-ray emission (Gunell et al., 2004) have all been studied using Martian plasma models. Transient processes including coronal mass ejection (CMEs; Dong, Ma, et al., 2015; Ma et al., 2017), changes in dynamic pressure (Ma et al., 2014), changes in solar extreme ultraviolet (EUV) flux (Modolo et al., 2006, 2005), seasonal variation (Dong et al., 2015), and crustal field rotation (Fang et al., 2015; Ma et al., 2014) have also been topics of study. Long-term Martian evolution has also been examined through estimation of early conditions and the corresponding escape rates (Terada et al., 2009).

The wide variety of models presents a unique challenge in cross-validation of results. In addition to different implementations and numerical methods, each model type makes different implicit physical assumptions. This means that the study of a particular plasma process may be more or less valid with the use of a particular model. The strengths and weaknesses of various models have been discussed previously in the literature (Ledvina et al., 2008). Directly comparing model results provides a complementary approach to the aforementioned discussion, to determine how the fundamental differences affect the interpretation of simulations.

Here we perform a model comparison challenge where we run a variety of models with the same input conditions to understand the strengths and weaknesses of each one. Running a model challenge allows the comparison across a variety of model types in a one-to-one manner and isolates the effects of different physics from the effects of the input conditions.

Model challenges are a commonly used tool across a variety of disciplines (e.g., Hurrell, 1995; Kim et al., 2016). Within the Martian modeling community, one such model challenge has previously been performed (Brain et al., 2010); however, substantial model development has occurred in the interim, and it is useful to provide an updated effort and expand the types of analysis performed. Here we evaluate different quantities, beyond boundaries and global escape rates. Additionally, we compare to Mars Atmospheric Volatile EvolutioN (MAVEN; Jakosky et al., 2015) data from a single orbit with upstream conditions that correspond to our model inputs. This provides a baseline measurement for comparison in the region of the spacecraft orbit. In particular, MAVEN adds critical information due to its simultaneous measurements of particles and fields.

In this paper we report the results from such a model comparison challenge. We identified a suitable MAVEN orbit, extracted the upstream solar wind drivers, and ran a variety of models using nearly identical input conditions. In section 2 we describe the input conditions and codes. Our results are shown in section 3, where we focus on the plasma boundaries (3.1), low-altitude ion behavior (3.2), southern hemisphere (3.3), and global escape (3.4). We conclude with a discussion and summary in section 4, as well as brief projection of our future work.

2. Methods

2.1. Orbit

This model challenge was designed such that the results can be compared to data from a specific MAVEN orbit. The trajectory of the chosen orbit (#2349, 14 December 2015) is depicted in Figure 1. The coordinates are labeled in the Mars Solar Orbital (MSO) coordinate system; $+\vec{x}$ is the direction from Mars to the Sun, $+\vec{z}$ is perpendicular to the orbital plane of Mars, and $+\vec{y}$ is the completion of a right-handed coordinate system. This orbit is almost entirely in the terminator plane, with periapsis near dawn at the equator. The subsolar longitude is 170°, indicating that the dominant crustal fields are on the dayside of the planet as the dominant crustal fields are centered around a geographic longitude of 180°.

Figure 1 also shows data from the Solar Wind Electron Analyzer (SWEA; Mitchell et al., 2016), Solar Wind Ion Analyzer (SWIA; Halekas et al., 2015), Suprathermal and Thermal Ion Composition (STATIC; McFadden et al., 2015), and the Magnetometer (MAG; Connerney et al., 2015) rotated into MSO coordinates. MAVEN exits and enters the upstream solar wind at times 17:12 and 20:24, respectively. At times 17:30–18:30 both STATIC and SWIA show a group of highly energetic ions whose energy increases with altitude in the northern hemisphere, commonly referred to as the ion plume. Periapsis occurs around 18:43 where many heavy ions are measured. The outbound portion of the orbit shows another section of heavy ions from times 19:05–19:25. The model results for these regions will be explored in section 3.

2.2. Upstream Boundary

The upstream boundary conditions (Table 1) were calculated from period of orbit #2349 MAVEN in the upstream solar wind and are listed in Table 1. These conditions are relatively moderate, not representing

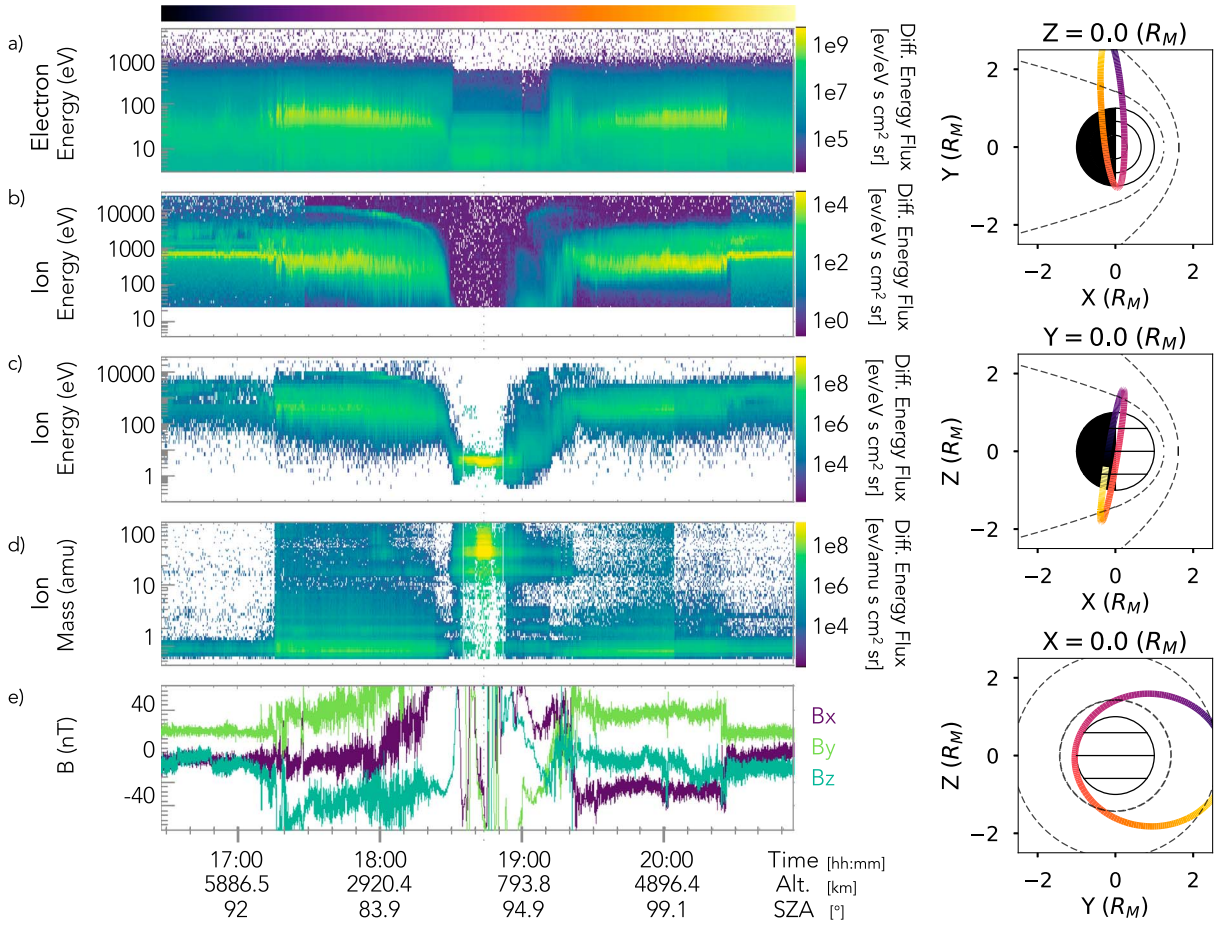

Figure 1. Trajectory and data from the MAVEN orbit (2349, 14 December 2015) that the upstream conditions are drawn from. (left) Panels show (a) electron flux per energy as measured by SWEA, (b) ion flux per energy as measured by SWIA, (c) ion flux per energy as measured by STATIC, (d) ion flux per mass as measured by STATIC, and (e) magnetic field as measured by MAG. The *x* axis is labeled by time, altitude, and Solar Zenith Angle (SZA). (right) Trajectory of MAVEN orbit in MSO coordinates. Empirical boundaries (Trotignon et al., 2006) are plotted as dashed lines, and the color corresponds to the time bar on the left.

an extreme event, and are consistent between the inbound and outbound portions of the orbit. The interplanetary magnetic field (IMF) is almost entirely in the $+\vec{y}$ direction, perpendicular to the solar wind velocity.

2.3. Models

As shown in Table 2, a wide variety of models were run for this model challenge, with different codes and underlying physical assumptions. Each model will be referred to by the tag given in the first column to minimize confusion between similar models. In this section we describe the models, some of the relevant implementation details, and any differences in the parameters used to run the simulations. Although multiple crustal field models were used, this will not cause a significant difference in the results.

2.3.1. MHD Models

The three MHD models were all run within the BATS-R-US (Block Adaptive-Tree Solar wind Roe-type Upwind Scheme) code (Glocer et al., 2009; Ma et al., 2004; Najib et al., 2011). The BATS-R-US platform has a nonuniform spherical grid to maximize resolution near the planet while minimizing computation time. The radial resolution varies from 10 to 600 km, and the angular resolution varies between 1.875 and 3.75. The simulated domain extends from −24 to +8 R_M (where R_M is the radius of Mars) in the *x* direction, and −16 to +16 in the *y* and *z* directions. Local time stepping is utilized such that the time step can vary dynamically between cells while satisfying the Courant condition.

Table 1
Upstream Conditions and Derived Parameters Extracted From MAVEN Data, Used to Drive the Models

v	[−350, 0, 0] km/s
n_p	4.9 cm^{-3}
n_α	0.14 cm^{-3}
T_p	59,200 K
B	[−0.74, 5.46, −0.97] nT
P_{dyn}	0.5 nPa
v_A	55 km/s

Note. Here P_{dyn} is the dynamical pressure and v_A is the Alfven speed.

Within this platform, three separate simulations were performed with increasing complexity. The first, BATSRUS-MS (Ma et al., 2004), is a multispecies run where ions H^+, O^+, O_2^+, and CO_2^+ were included and treated as a single fluid. This model solves a single momentum and energy equation but separate continuity equations for each species. BATSRUS-MF, the second model (Najib et al., 2011), includes the same ion species, but each species is treated as a separate fluid with its own continuity and momentum equations. BATSRUS-MF+Pe (Ma et al., 2013) includes the same ion species as independent fluids and also solves an equation for the electron pressure analogous to the energy equation that dictates ion pressure (see details in Ma et al., 2011), allowing the electron temperature to differ from the ion temperature.

For all three simulations the lower boundary of the code is set at 100 km above the planet, and the O^+, O_2^+, and CO_2^+ densities are set by the photoequilibrium values. The velocity condition at the lower boundary is reflexive, leading to an approximately zero value. Crustal fields were included as modeled by Arkani-Hamed (2001).

2.3.2. Hybrid Models

The two hybrid simulations were run using two different codes: HELIOSARES (Modolo et al., 2016), and RHybrid (Jarvinen et al., 2018). As hybrid codes they both treat ions as macroparticles that evolve kinetically according to the Lorentz force, while the electrons are implemented as a charge neutralizing fluid. A macroparticle does not represent a single physical particle, rather a group of particles with a given density and the same properties. Fields are advanced by accumulating particle moments according to macroparticle shape functions onto a grid using a cloud-in-cell technique and then solving the magnetic and electric field equations accordingly. In order to improve particle statistics, multiple independent time steps were averaged together to create the data sets that were analyzed here. Both models include planetary H^+, O^+, O_2^+, He^{++}, and H^+. Although CO_2+ is included in the HELIOSARES simulation, due to the limited resolution compared to the ion scale height, it is not included in further analysis. The RHybrid run analyzed here does not include CO_2+.

This HELIOSARES run uses a Cartesian grid with a resolution of 60 km and a lower boundary at 110 km, and bounds $X = [-2.7R_M, 2.1R_M]$, $Y, Z = \pm 4.7R_M$. Crustal fields are included via the Cain et al. (2003) model. HELIOSARES also implements a particle-splitting technique to limit numerical noise that results from having large particles; when a macroparticle with a statisical weight ≥3 times the solar wind density exceeds 700 km in altitude, it is split into two child particles with the same velocity and half the statistical weight. Solar wind and ionospheric electrons are modeled as two separate fluids, with densities set by the solar wind ion density and ionospheric ion density, respectively. The solar wind electron population is assumed to be adiabatic with polytropic index $\gamma_{\text{sw}} = 5/3$, while the ionospheric population follows a polytropic equation varying smoothly between isobaric and adiabatic as $\gamma_{\text{ion}} = a(1 + (a/\gamma_{\text{sw}})^4)^{-1/4}$ where $a = (\log(n_e))^{-1}$ and n_e is the ionospheric electron density.

To initialize the simulation, ion macroparticles are loaded to match ionospheric profiles computed assuming photoequilibrium. For the first 2,500 time steps, planetary ion motion is inhibited to allow a bow shock to develop before direct interaction of the solar wind with the ionosphere. Additionally, this HELIOSARES run was simulated using a different thermosphere, exosphere, and photoionization rates than are discussed in section 2.4. Full 3-D models for the exosphere and thermosphere generated for solar median, LS = 90 using

Table 2
A Summary of the Models Used in this Model Challenge Along With Some of the Relevant Parameters

	Model type	Crustal fields	Highest resolution (km)	Inner boundary (km)
BATSRUS-MS[a]	MHD	Yes	10	100
BATSRUS-MF[b]	MHD	Yes	10	100
BATSRUS-MF+PE[c]	MHD	Yes	10	100
HELIOSARES[d]	Hybrid	Yes	60	110
RHybrid[e]	Hybrid	No	113	300

Note. For reference, scale heights for O^+, O_2^+, and CO_2^+ are 40 km, 20 km, and 10 km, respectively.
[a]Ma et al. (2004), [b]Najib et al. (2011), [c]Ma et al. (2013), [d]Modolo et al. (2016), and [e]Jarvinen et al. (2018).

Laboratoire de Météorologie Dynamique Martian General Circulation Model (LMD-MGCM; González-Galindo et al., 2007), were utilized. Although they are not identical to the models used for the rest of the simulations, they are similar when averaged radially and should not greatly affect the presented results. The photoproduction is based on the EUVAC (EUV model for Aeronomic Calculations) model (Richards et al., 1994), which takes into account 27 wavelength groups, combined with the ionization and absorption cross sections for each species from Schunk and Nagy (2000). The computed photoionization frequencies are similar, with less than 20% difference from the other models.

This RHybrid run uses a Cartesian grid with a resolution of 113 km, bounds $X, Y, Z = \pm 4R_M$, and does not include crustal fields. Resistivity and electron velocity are set as zero at the altitude of 300 km and below. All ions are absorbed and removed from the simulation at the altitude of 200 km and below. Ionospheric O^+ and O_2^+ ions are emitted upward from a spherical shell at 400 km with the temperature of 2×10^4 K. The emission has a maximum flux at noon and cos(SZA) (Solar Zenith Angle) dependence toward terminator where the flux reaches 10% of the noon value and is constant for the nightside. Total ionospheric emission rates are 1.4×10^{25} s^{-1} for O^+ and 2×10^{25} s^{-1} for O_2^+. Photoionization of the exospheric monatomic oxygen and hydrogen neutral coronas are included at the altitude of 400 km and above in the dayside. The total photoionization rate in the simulation domain is 2.15×10^{24} s^{-1} for hydrogen and 2.67×10^{23} s^{-1} for monatomic oxygen. The exospheric neutral profiles and ionospheric emission rates are the same as in earlier studies such as Brain et al. (2010) and Jarvinen et al. (2016).

2.4. Inner Boundary

For all models except HELIOSARES, a 3-D neutral atmosphere and 1-D exosphere were used. The 3-D neutral atmosphere was computed using the Mars Global Ionosphere-Thermosphere Model (MGITM; Bougher et al., 2015) for an areocentric longitude of the Sun (LS) of 90° at moderate EUV ($F_{10.7} = 130$). MGITM uses Martian physical parameters, ion-neutral chemistry, and radiative processes in order to simulate the dynamical structure of Mars from the surface to the exosphere. The exosphere is implemented via 1-D profiles for hydrogen (Chaufray et al., 2008) and oxygen (Lee et al., 2015), with oxygen containing both a hot and cold component. Photoionization rates were also calculated using MGITM, and the additional rate coefficients were set from Schunk and Nagy (2000).

3. Results

3.1. Boundaries

The interaction of the solar wind with the Martian plasma environment produces several boundaries and transitions within the plasma, including the bow shock, and the transition region including the Magnetic Pileup Boundary (MPB) due to the pileup of the IMF as it drapes around the planet and the Induced Magnetosphere Boundary (IMB) marked by a transition from solar wind to planetary plasma (Nagy et al., 2004).

Figure 2 shows slices of H^+, O^+, and magnetic field magnitude in the $Y = 0$ and $Z = 0$ planes for each model. Overplotted in white are the locations of the empirical bow shock and MPB boundaries (Trotignon et al., 2006).

Each model well predicts the magnetic standoff distance and the position of the bow shock along the Mars-Sun line. Along the wings of the bow shock the H^+ and magnetic field magnitude slices show that all the BATSRUS models show a more extended shock region than the conic fits, while both hybrid models show a more compressed shock region. The shock boundary in the fluid models is symmetric with respect to Y and Z. This general lack of asymmetry is driven by an almost entirely $+y$-oriented IMF.

The HELIOSARES bow shock is more compressed in the $+\vec{z}$ hemisphere than in the $-\vec{z}$ hemisphere, driven by the electron pressure gradient and motional electric field, which points inward in the $-\vec{z}$ hemisphere and outward in $+\vec{z}$ hemisphere. As described in Simon et al. (2007), these two forces lead to the formation of a sharply pronounced boundary layer in the hemisphere where they are antiparallel. This effect is present in simulations that treat the ions kinetically, so is not present in the MHD models. RHybrid also shows asymmetry due to the motional electric field, but it is less pronounced in the $y = 0$ plane compared to HELIOSARES.

The transition to planetary plasma (depicted by O^+) along the subsolar line occurs simultaneously with the empirical boundary location for all models. In the X-Z plane (Figure 2a), the BATSRUS-MS and BATSRUS-Pe models show little asymmetry in O^+ number density and well reproduce the empirical boundary location,

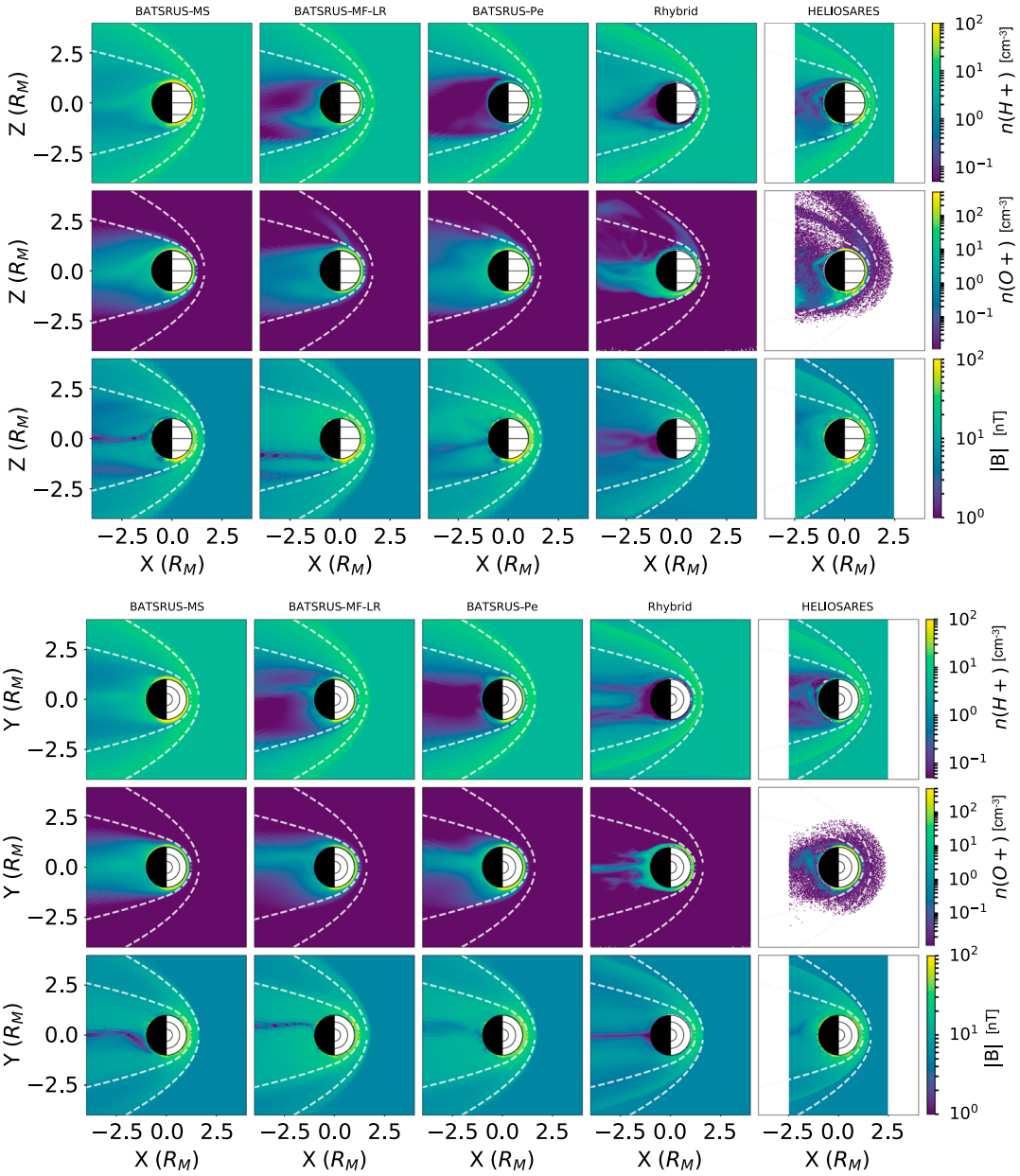

Figure 2. Slices in the *XZ* (top) and *XY* (bottom) planes. From top to bottom the rows show H^+ number density, O^+ number density, and magnetic field magnitude. The columns indicate the model, from left to right: BATSRUS-MS, BATSRUS-MF, BATSRUS-MF+Pe, RHybrid, and HELIOSARES. The empty space in the HELIOSARES data occurs because a slightly smaller domain is simulated while the plotting limits are kept constant. Each column uses identical color space limits.

while BATSRUS-MF and HELIOSARES show strong *Z* asymmetry, and RHybrid only shows planetary plasma along the plume and current sheet outside the ionosphere. All models show very little asymmetry in the *X*-*Y* plane (Figure 2b).

Figure 3 confirms the intuition gained with slices, but by flying through the models we are also able to compare with MAVEN data from this orbit. On the inbound portion of the orbit the MAVEN data show a bow shock at roughly the same location as the empirical boundary, but the outbound crossing happens lower in altitude than the empirical crossing. This indicates the presence of some combination of asymmetry and time variability. As the shocked region is relatively extended in the MHD models, none of them show a bow shock crossing in this flythrough; instead, MAVEN's orbit encounters only modeled magnetosheath and lower. Thus, both the H^+ number density and the magnetic field magnitude appear to be larger in the fluid models than

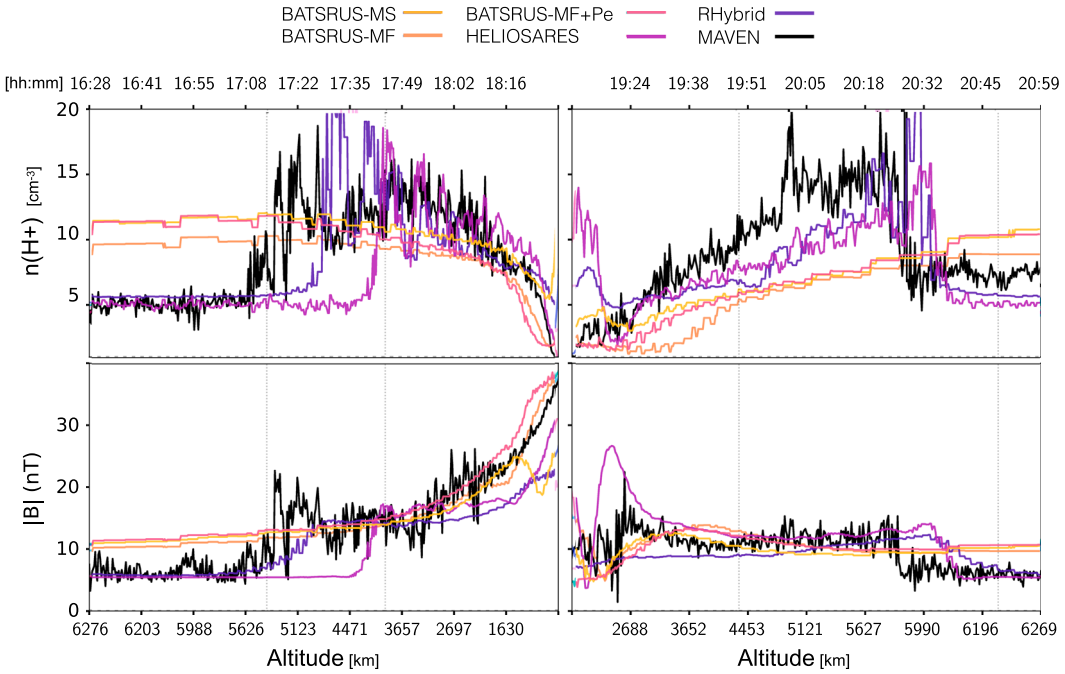

Figure 3. Flythrough of model results of the inbound and outbound portions of the orbit (#2349, 14 December 2015) excluding periapsis with corresponding MAVEN data. Panels show H^+ number density and magnetic field magnitude. The location at which the orbit passes through the analytic boundary locations (Trotignon et al., 2006) for the bow shock and MPB/IMB are plotted as vertical dashed lines.

the data and hybrid models. The RHybrid and HELIOSARES models both show a clear shock crossing that is lower in altitude than the inbound MAVEN crossing, but very similar on the outbound crossing.

3.2. Low Altitude

MAVEN enters the ionosphere on Mars' northern hemisphere along the terminator plane. Measurements in this region from the Neutral Gas and Ion Mass Spectrometer (NGIMS; Mahaffy et al., 2015) are shown along with model results in Figure 4. RHybrid is not shown here due to the absence of ionosphere in the run.

At the lowest altitudes there is strong agreement across all models and data for O^+, O_2^+, and CO_2^+, indicating that the ion production physics is well represented in each model. Previous studies, including Ma et al. (2015) also found good agreement in ionospheric densities between data and models. The difference in shapes of the heavy ion profiles are indicative of different dominant heights. The relative steepness in decline with altitude between ions and the shape of the distributions are consistent with predicted scale heights. The jaggedness of the HELIOSARES profiles is due to the limited resolution of the grid that the ion macroparticles are deposited onto. The shallow drop off of the HELIOSARES densities on the outbound segment relative to the inbound segment is due to contributions from the southern hemisphere's slow escaping ions (see section 3.3).

For each ion, the inbound portion of the MAVEN data shows some excess number density relative to the steep drop off shown by the models, likely due to time and spatial variability not captured by the models.

3.3. Southern Hemisphere

Cold ion escape likely plays an important role in heavy ion loss on Mars (Dong, Fang et al., 2015; Fränz et al., 2015). Here we discuss differences between the models in the southern ($-z$) hemisphere where an extended population of cold ions connects to the tail. This region of the tail is not affected by the northern pickup ions, which we will discuss in a future paper.

As shown in Figure 5, all models show a region of planetary ions that extends from the southern hemisphere toward the tail. These ions are cold and have near-zero bulk velocity. HELIOSARES shows slightly higher number densities than the BATSRUS and RHybrid models, and the region extends farther in the $-z$ direction.

Figure 5 also shows vectors of the magnetic field. From this figure it is clear that the topology varies substantially in this region across the models. The top row shows a draped field configuration in the BATSRUS

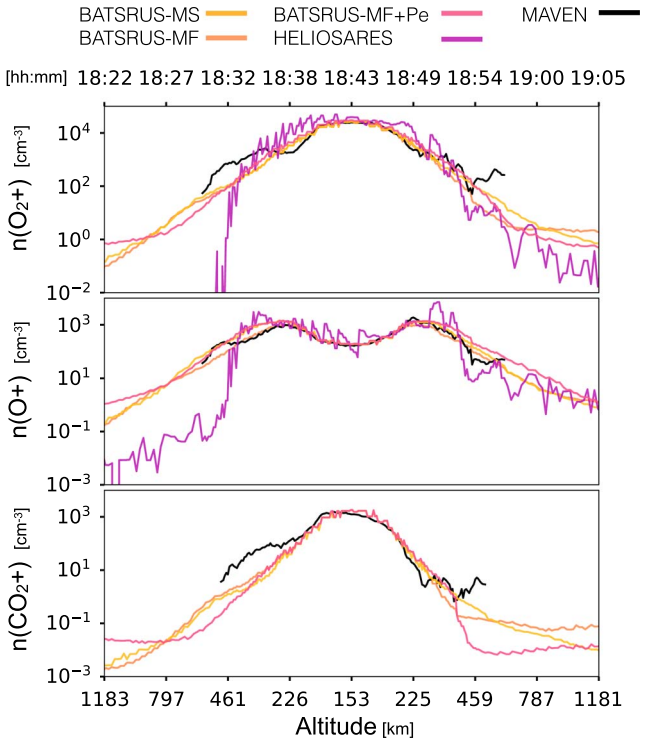

Figure 4. Flythrough of model results at low altitudes with corresponding MAVEN data from orbit #2349, 14 December 2015). Panels show O_2^+, O^+, CO_2^+ number densities from top to bottom. RHybrid results are excluded due to the lack of ionosphere. No HELIOSARES results are shown for CO_2^+ because it was not included in the model.

and RHybrid models, while the field in the HELIOSARES model appears toroidal where the ion densities are highest. In the *YZ* plane (middle row) the HELIOSARES model again appears toroidal in the tail, while the BATSRUS models all show magnetic field vectors predominately in the $\pm x$ direction.

From examining the field line topology in three dimensions the magnetic field in HELIOSARES appears coiled in the southern hemisphere, forming a channel for slow ion escape. This differs from the magnetic topology in BATSRUS, which appears more like a basic current sheet model created by a draped IMF. These differences are likely related to differences in the obstacle boundary and conductivity.

3.4. Global Escape

One of the foremost areas of interest to the Martian community is the rate at which ions are lost to space, and the channels this escape proceeds through. Global ion escape has been measured (Barabash et al., 2007; Lundin et al., 1989), as has variance in escape with solar wind and EUV (Ramstad et al., 2015), and variance with crustal fields (Ramstad et al., 2016); for full review of global ion escape at Mars see Dubinin et al. (2011). Brain et al. (2015) has mapped the spatial distribution of inflowing and outflowing ion fluxes by averaging data across many orbits. Here we present similar maps to Brain et al. (2015) but of the entire system at a single instance in time as simulated by the models.

Figure 6 shows maps of the modeled ion fluxes at $1.8R_M$ across latitude and longitude in the Mars-Solar-Electric field (MSE) coordinate system; $+\vec{x}$ is the direction from Mars to the Sun, $+\vec{z}$ is along the upstream solar wind motional electric field, and $+\vec{y}$ is the completion of a right-handed coordinate system. The maps are created by defining a set of points in a spherical shell, equally spaced in 5° increments in latitude and longitude, and probing the net ion flux at each point in each model without averaging or interpolation.

On the dayside (centered on longitude = 0), all models have inbound heavy ion flux. In BATSRUS-MS this is symmetrical around latitude = 0 and longitude = 0. In the BATSRUS-MF, BATSRUS-MF+Pe, RHybrid, and HELIOSARES models the dayside inbound ion flux is confined to the southern hemisphere.

This symmetry breaking is related to the plume presence in the BATSRUS-MF, BATSRUS-MF+Pe, RHybrid, and HELIOSARES models. The plume feature is seen as a dark blue (outbound flux) feature at high latitudes

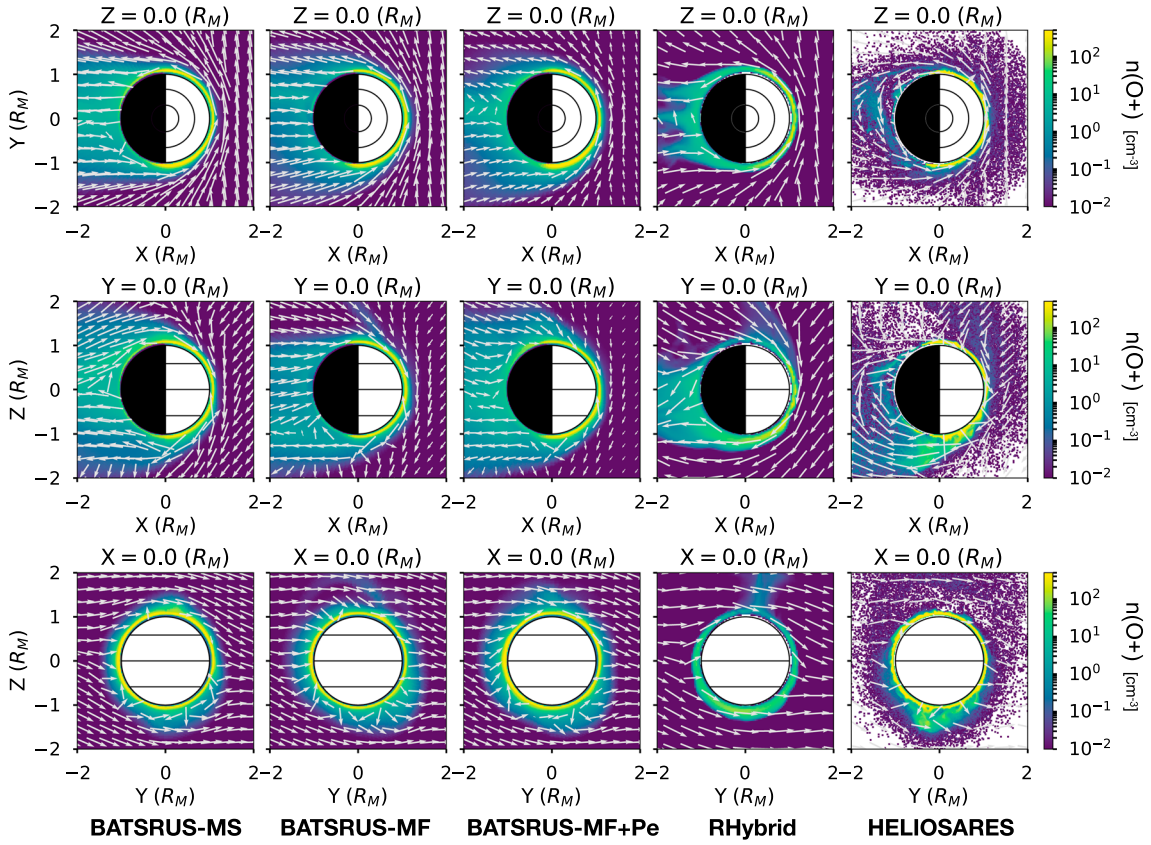

Figure 5. Slices of O^+ number density with magnetic field vectors overlaid. Panels show (top to bottom) planes $Z = -1.3R_M$, $Y = 0$, $X = 0$, and (left to right) simulations BATSRUS-MS, BATSRUS-MF, BATSRUS-MF+Pe, RHybrid, and HELIOSARES. All color bars are consistent and labeled to the right.

(>45° directly above the northern pole) centered around longitude −30°, and as a channel connecting to the tailward outbound flux centered at longitude 180°. Furthermore, due to the limited number of heavy ions at large radii on the dayside, the H^+ dynamics dictate the ion flux for BATSRUS-MS.

All models except HELIOSARES show predominately outbound flux in the tail. RHybrid shows only outbound flux, while all the BATSRUS models have regions where ions are inflowing. These inflow regions are present in the same locations at lower altitudes (down to $1.1R_M$) but shrink at higher altitudes out to ~3.0 R_M). They are also correlated to the magnetic field vector at this point. This indicates that they are likely related to the dynamics of the current sheet and the presence of crustal fields, as only RHybrid does not include crustal fields. As the dynamics of these regions are sensitive to tail plasma processes, crustal field implementation, and low-altitude nightside ions, and our orbit does not probe this region, we leave further study to future work.

We find that the modeled maps are qualitatively similar to maps created from MAVEN data (Brain et al., 2015). The dayside shows predominately inward flux, while the tail shows outward flux. Northern MSE latitude shows relatively more outward flux than the southern MSE latitude region. However, coverage of this space is still relatively incomplete due to the limited amount of MAVEN orbits there have been, so further conclusions and more detailed model-data comparison are not yet possible.

By summing across all latitude/longitude bins and weighting by area, global ion fluxes can be calculated for a given radius for each model. The rates for $R = 1.8R_M$ are shown in Table 3, along with observed rates calculated by Brain et al. (2015) and Ramstad et al. (2015). A full comparison with all observed rates is beyond the scope of this paper, we just show Brain et al. (2015) for comparison with the escape maps and Ramstad et al. (2015) for a recent result calculated for comparable solar wind conditions. For a full comparison of ion escape rates at Mars, see Dubinin et al. (2011).

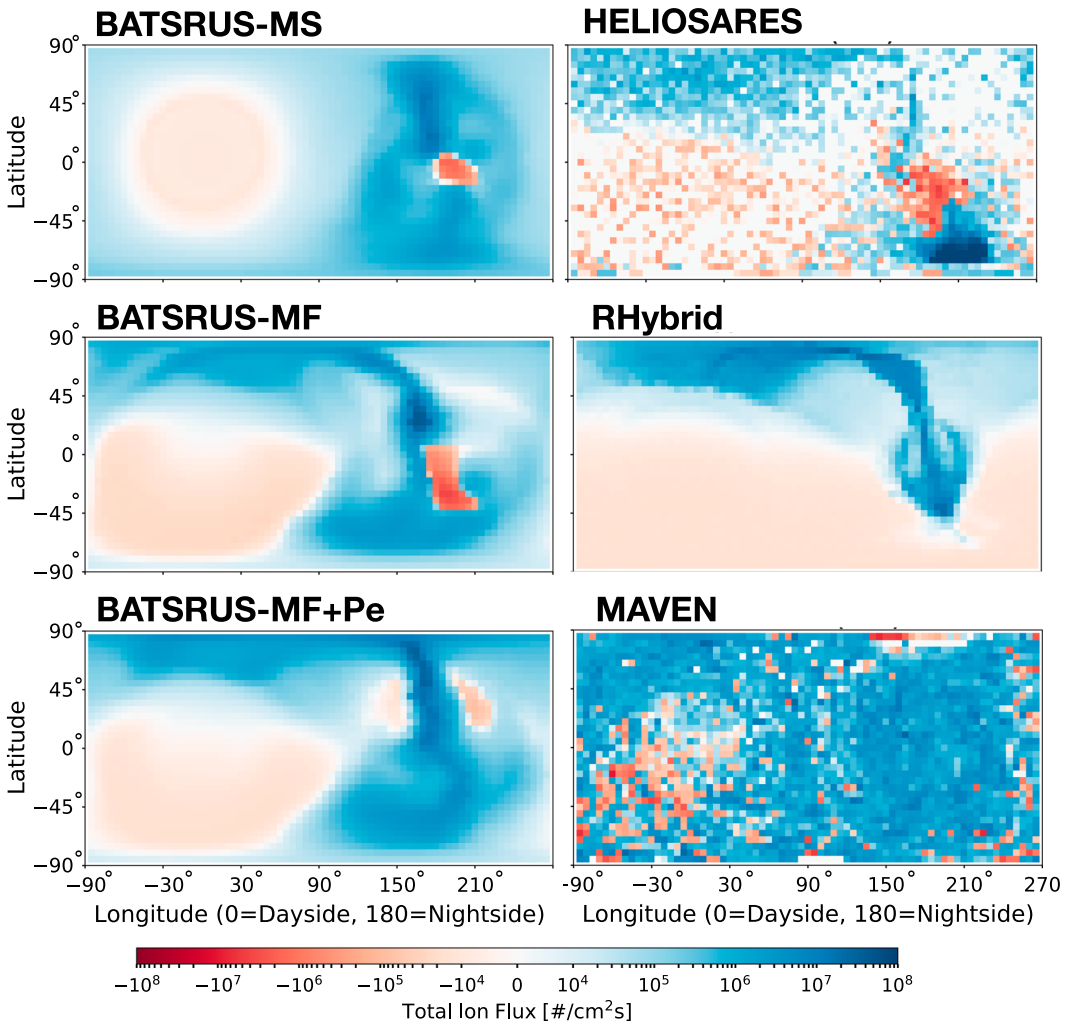

Figure 6. Total heavy ion flux maps for (left to right, top to bottom) BATSRUS-MS, RHybrid, BATSRUS-MF+Pe, BATSRUS-MF+Pe, HELIOSARES, and MAVEN data. Axes limits and color bar are identical for each panel (except the MAVEN panel which is labeled separately), with blue indicating outward flux and red indicating inward flux. The map created from MAVEN data is adopted from Brain et al. (2015).

Table 3
Calculated and Observed Escape Rates for O^+, O_2^+, and Total

Model/Survey	O^+ ($\times 10^{24}$ #/s)	O_2^+ ($\times 10^{24}$ #/s)	Total ($\times 10^{24}$ #/s)
BATSRUS-MS	1.0	1.1	2.1
BATSRUS-MF	0.6	1.8	2.4
BATSRUS-MF+Pe	1.3	2.1	3.4
RHybrid	1.1	1.1	2.2
HELIOSARES	2.3	0.9	3.2
Brain et al. (2015)	–	–	1.6
Ramstad et al. (2015)	–	–	2.1 ± 1.1

Note. For each model the total includes all species included in the model, while the total for the observed rates includes all ions with energies above the relevant cutoff.

These results are very constant with radius for all models and are very similar for such a large variation in escape maps. There is greater agreement between these rates than those calculated by Brain et al. (2010), indicating some level of convergence over time across models. These rates are also within a factor of 3 of those calculated by Brain et al. (2015), though those rates are for a wide variety of solar wind conditions and planetary orientation and also include all heavy ion species. When compared to rates calculated by Ramstad et al. (2015) for similar solar wind and EUV conditions our calculated rates are all within the appropriate range ($2.1 \pm 1.1 \times 10^{24}$ s^{-1}).

4. Conclusion

Five models of the Martian magnetosphere have been run for nearly identical input conditions (aside from the small variations discussed in section 2); these models were then compared to each other and to MAVEN data. The input conditions were chosen to reflect the upstream drivers of MAVEN orbit #2349, an orbit chosen because the solar wind data is steady and typical, while the rest of the orbit probes other interesting regions. Model flythroughs along the orbit trajectory, slices through different regions, spherical ion flux maps, and global escape rates were obtained for each data set.

Most models showed little boundary asymmetry due to the IMF being nearly completely in the $+\vec{y}$ direction. The overall extent of the shocked region was larger in the fluid models than both the empirical boundaries and the MAVEN results, while the hybrid models matched the outbound crossing very well.

From comparing NGIMS ion data to model flythroughs at low altitude it is clear that all models that have an inner boundary lower than ~200 km do a good job modeling the low-altitude dayside ions. Both overall normalization and scale heights are well recreated by all the BATSRUS models as well as HELIOSARES.

The outflow of cold ions in the southern hemisphere varied substantially across models. More study of the effects of lower boundary conditions and the impact they have on the magnetic topology and ion outflow in tail could impact ion escape estimates. However, although this outflow was much denser and more localized in the HELIOSARES model than the BATSRUS models, overall global escape rates were relatively constant.

Future efforts on this front are still necessary. This model challenge focused specifically on one orbit with a moderate solar wind and +*y* directed IMF. Changing input conditions will vary how the solar wind interacts with the ionosphere and likely how variations in model physics appear. Furthermore, we have limited our analysis to certain regions and delayed comparison of the plume region for a future paper. More analysis and comparisons with data from additional MAVEN orbits will be necessary to probe other regions such as the tail.

Acknowledgments
The MAVEN project is supported by NASA through the Mars Exploration Program, and MAVEN data are publicly available through the Planetary Data System. The work of H. E. was supported by the DOE Computational Science Graduate Fellowship. The work of R. J. was supported by the Academy of Finland (Decision 257831). The RHybrid simulation run was performed using the RHybrid simulation platform distributed under an open source license by the Finnish Meteorological Institute (https://github.com/fmihpc/rhybrid). C. F. Dong is supported by the NASA Living With a Star Jack Eddy Postdoctoral Fellowship Program, administered by the University Corporation for Atmospheric Research. All 1-D and 2-D data products used for the figures contained in this paper are available on the MAVEN SDC website (https://lasp.colorado.edu/maven/sdc/public/).

References

Arkani-Hamed, J. (2001). A 50-degree spherical harmonic model of the magnetic field of Mars. *Journal of Geophysical Research*, *106*, 23,197–23,208. https://doi.org/10.1029/2000JE001365

Barabash, S., Fedorov, A., Lundin, R., & Sauvaud, J.-A. (2007). Martian atmospheric erosion rates. *Science*, *315*, 501–503. https://doi.org/10.1126/science.1134358

Bertucci, C., Mazelle, C., Acuña, M., Russell, C., & Slavin, J. (2005). Structure of the magnetic pileup boundary at Mars and Venus. *Journal of Geophysical Research*, *110*, A01209. https://doi.org/10.1029/2004JA010592

Bößwetter, A., Bagdonat, T., Motschmann, U., & Sauer, K. (2004). Plasma boundaries at Mars: A 3-D simulation study. *Annales Geophysicae*, *22*, 4363–4379. https://doi.org/10.5194/angeo-22-4363-2004

Boesswetter, A., Lammer, H., Kulikov, Y., Motschmann, U., & Simon, S. (2010). Non-thermal water loss of the early Mars: 3D multi-ion hybrid simulations. *Planetary and Space Science*, *58*, 2031–2043. https://doi.org/10.1016/j.pss.2010.10.003

Bougher, S. W., Pawlowski, D., Bell, J. M., Nelli, S., McDunn, T., Murphy, J. R., et al. (2015). Mars global ionosphere-thermosphere model: Solar cycle, seasonal, and diurnal variations of the Mars upper atmosphere. *Journal of Geophysical Research: Planets*, *120*, 311–342. https://doi.org/10.1002/2014JE004715

Brain, D., Barabash, S., Boesswetter, A., Bougher, S., Brecht, S., Chanteur, G., et al. (2010). A comparison of global models for the solar wind interaction with Mars. *Icarus*, *206*, 139–151. https://doi.org/10.1016/j.icarus.2009.06.030

Brain, D., McFadden, J. P., Halekas, J. S., Connerney, J. E. P., Bougher, S. W., Curry, S., et al. (2015). The spatial distribution of planetary ion fluxes near Mars observed by MAVEN. *Geophysical Research Letters*, *42*, 9142–9148. https://doi.org/10.1002/2015GL065293

Brecht, S. H., & Ledvina, S. A. (2014). The role of the Martian crustal magnetic fields in controlling ionospheric loss. *Geophysical Research Letters*, *41*, 5340–5346. https://doi.org/10.1002/2014GL060841

Brecht, S. H., Ledvina, S. A., & Bougher, S. W. (2016). Ionospheric loss from Mars as predicted by hybrid particle simulations. *Journal of Geophysical Research: Space Physics*, *121*, 10,190–10,208. https://doi.org/10.1002/2016JA022548

Cain, J. C., Ferguson, B. B., & Mozzoni, D. (2003). An $n = 90$ internal potential function of the Martian crustal magnetic field. *Journal of Geophysical Research*, *108*(E2), 5008. https://doi.org/10.1029/2000JE001487

Chanteur, G. M., Dubinin, E., Modolo, R., & Fraenz, M. (2009). Capture of solar wind alpha-particles by the Martian atmosphere. *Geophysical Research Letters*, *36*, L23105. https://doi.org/10.1029/2009GL040235

Chaufray, J. Y., Bertaux, J. L., Leblanc, F., & Quémerais, E. (2008). Observation of the hydrogen corona with SPICAM on Mars Express. *Icarus*, *195*, 598–613. https://doi.org/10.1016/j.icarus.2008.01.009

Connerney, J. E. P., Espley, J., Lawton, P., Murphy, S., Odom, J., Oliversen, R., & Sheppard, D. (2015). The MAVEN magnetic field investigation. *Space Science Reviews*, *195*, 257–291. https://doi.org/10.1007/s11214-015-0169-4

Cravens, T. E., Hoppe, A., Ledvina, S. A., & McKenna-Lawlor, S. (2002). Pickup ions near Mars associated with escaping oxygen atoms. *Journal of Geophysical Research*, *107*(A8), 1170. https://doi.org/10.1029/2001JA000125

Dong, C., Bougher, S. W., Ma, Y., Toth, G., Lee, Y., Nagy, A. F., et al. (2015). Solar wind interaction with the Martian upper atmosphere: Crustal field orientation, solar cycle, and seasonal variations. *Journal of Geophysical Research: Space Physics*, *120*, 7857–7872. https://doi.org/10.1002/2015JA020990

Dong, C., Ma, Y., Bougher, S. W., Toth, G., Nagy, A. F., Halekas, J. S., et al. (2015). Multifluid MHD study of the solar wind interaction with Mars' upper atmosphere during the 2015 March 8th ICME event. *Geophysical Research Letters*, *42*, 9103–9112. https://doi.org/10.1002/2015GL065944

Dong, Y., Fang, X., Brain, D. A., McFadden, J. P., Halekas, J. S., Connerney, J. E., et al. (2015). Strong plume fluxes at Mars observed by MAVEN: An important planetary ion escape channel. *Geophysical Research Letters*, *42*, 8942–8950. https://doi.org/10.1002/2015GL065346

Dryer, M., & Heckman, G. (1967). On the hypersonic analogue as applied to planetary interaction with the solar plasma. *Planetary and Space Science*, *15*, 515–546.

Dubinin, E., Fraenz, M., Fedorov, A., Lundin, R., Edberg, N., Duru, F., & Vaisberg, O. (2011). Ion energization and escape on Mars and Venus. *Space Science Reviews*, *162*, 173–211. https://doi.org/10.1007/s11214-011-9831-7

Fang, X., Liemohn, M. W., Nagy, A. F., Luhmann, J. G., & Ma, Y. (2010). On the effect of the Martian crustal magnetic field on atmospheric erosion. *Icarus*, *206*, 130–138. https://doi.org/10.1016/j.icarus.2009.01.012

Fang, X., Liemohn, M. W., Nagy, A. F., Ma, Y., De Zeeuw, D. L., Kozyra, J. U., & Zurbuchen, T. H. (2008). Pickup oxygen ion velocity space and spatial distribution around Mars. *Journal of Geophysical Research*, *113*, a02210. https://doi.org/10.1029/2007JA012736

Fang, X., Ma, Y., Brain, D., Dong, Y., & Lillis, R. (2015). Control of Mars global atmospheric loss by the continuous rotation of the crustal magnetic field: A time-dependent MHD study. *Journal of Geophysical Research: Space Physics*, *120*, 10,926–10,944. https://doi.org/10.1002/2015JA021605

Fränz, M., Dubinin, E., Andrews, D., Barabash, S., Nilsson, H., & Fedorov, A. (2015). Cold ion escape from the Martian ionosphere. *Planetary and Space Science*, *119*, 92–102. https://doi.org/10.1016/j.pss.2015.07.012

Glocer, A., Tóth, G., Ma, Y., Gombosi, T., Zhang, J.-C., & Kistler, L. M. (2009). Multifluid block-adaptive-tree solar wind Roe-type upwind scheme: Magnetospheric composition and dynamics during geomagnetic storms—Initial results. *Journal of Geophysical Research*, *114*, A12203. https://doi.org/10.1029/2009JA014418

González-Galindo, F., Forget, F., López-Valverde, M. A., Angelats I Coll, M., & Bougher, S. W. (2007). LMD-MGCM: The first ground-to-exosphere general circulation model of the Martian atmosphere. In *Seventh International Conference on Mars*, LPI Contributions, No. 1353, Pasadena, California, pp. 3099.

Gunell, H., Holmström, M., Barabash, S., Kallio, E., Janhunen, P., Nagy, A. F., & Ma, Y. (2006). Planetary ENA imaging: Effects of different interaction models for Mars. *Planetary and Space Science*, *54*, 117–131. https://doi.org/10.1016/j.pss.2005.04.002

Gunell, H., Holmström, M., Kallio, E., Janhunen, P., & Dennerl, K. (2004). X rays from solar wind charge exchange at Mars: A comparison of simulations and observations. *Geophysical Research Letters*, *31*, L22801. https://doi.org/10.1029/2004GL020953

Halekas, J. S., Taylor, E. R., Dalton, G., Johnson, G., Curtis, D. W., McFadden, J. P., et al. (2015). The solar wind ion analyzer for MAVEN. *Space Science Reviews*, *195*, 125–151. https://doi.org/10.1007/s11214-013-0029-z

Harnett, E. M., & Winglee, R. M. (2007). High-resolution multifluid simulations of the plasma environment near the Martian magnetic anomalies. *Journal of Geophysical Research*, *112*, a05207. https://doi.org/10.1029/2006JA012001

Holmstrom, M., & Wang, X.-D. (2015). Mars as a comet: Solar wind interaction on a large scale. *Planetary and Space Science*, *119*, 43–47. https://doi.org/10.1016/j.pss.2015.09.017

Hurrell, J. W. (1995). Comparison of NCAR community climate model (CCM) climates. *Climate Dynamics*, *11*(1), 25–50. https://doi.org/10.1007/BF00220675

Jakosky, B. M., Lin, R. P., Grebowsky, J. M., Luhmann, J. G., Mitchell, D. F., Beutelschies, G., et al. (2015). The Mars Atmosphere and Volatile Evolution (MAVEN) mission. *Space Science Reviews*, *195*, 3–48. https://doi.org/10.1007/s11214-015-0139-x

Jarvinen, R., Brain, D. A., & Luhmann, J. G. (2016). Dynamics of planetary ions in the induced magnetospheres of Venus and Mars. *Planetary and Space Science*, *127*, 1–14. https://doi.org/10.1016/j.pss.2015.08.012

Jarvinen, R., Brain, D., Modolo, R., Fedorov, A., & Holmström, M. (2018). Oxygen ion energization at Mars: Comparison of MAVEN and Mars Express observations to global hybrid simulation. *Journal of Geophysical Research: Space Physics*, *123*, 1678–1689. https://doi.org/10.1002/2017JA024884

Kallio, E., Barabash, S., Brinkfeldt, K., Gunell, H., Holmström, M., Futaana, Y., et al. (2006). Energetic neutral atoms (ENA) at Mars: Properties of the hydrogen atoms produced upstream of the Martian bow shock and implications for ENA sounding technique around non-magnetized planets. *Icarus*, *182*(2), 448–463. https://doi.org/10.1016/j.icarus.2005.12.019

Kallio, E., Fedorov, A., Budnik, E., Säles, T., Janhunen, P., Schmidt, W., et al. (2006). Ion escape at Mars: Comparison of a 3-D hybrid simulation with Mars Express IMA/ASPERA-3 measurements. *Icarus*, *182*(2), 350–359. https://doi.org/10.1016/j.icarus.2005.09.018

Kallio, E., & Janhunen, P. (2002). Ion escape from Mars in a quasi-neutral hybrid model. *Journal of Geophysical Research*, *107*(A3), 1035. https://doi.org/10.1029/2001JA000090

Kim, J.-H., Agertz, O., Teyssier, R., Butler, M. J., Ceverino, D., Choi, J.-H., et al. (2016). The AGORA high-resolution galaxy simulations comparison project. II. Isolated disk test. *Astrophysical Journal*, *833*, 202. https://doi.org/10.3847/1538-4357/833/2/202

Ledvina, S., Ma, Y., & Kallio, E. (2008). Modeling and simulating flowing plasmas and related phenomena. *Space Science Reviews*, *139*(1–4), 143–189. https://doi.org/10.1007/s11214-008-9384-6

Lee, Y., Combi, M. R., Tenishev, V., Bougher, S. W., & Lillis, R. J. (2015). Hot oxygen corona at Mars and the photochemical escape of oxygen: Improved description of the thermosphere, ionosphere, and exosphere. *Journal of Geophysical Research: Planets*, *120*, 1880–1892. https://doi.org/10.1002/2015JE004890

Liemohn, M. W., Curry, S. M., Fang, X., & Ma, Y. (2013). Comparison of high-altitude production and ionospheric outflow contributions to O^+ loss at Mars. *Journal of Geophysical Research: Space Physics*, *118*, 4093–4107. https://doi.org/10.1002/jgra.50388

Liemohn, M. W., Ma, Y., Frahm, R. A., Fang, X., Kozyra, J. U., Nagy, A. F., et al. (2006). Mars global MHD predictions of magnetic connectivity between the dayside ionosphere and the magnetospheric flanks. *Space Science Reviews*, *126*, 63–76. https://doi.org/10.1007/s11214-006-9116-8

Lundin, R., Zakharov, A., Pellinen, R., Borg, H., Hultqvist, B., Pissarenko, N., et al. (1989). First measurements of the ionospheric plasma escape from Mars. *Nature*, *341*, 609–612. https://doi.org/10.1038/341609a0

Ma, Y., Fang, X., Russell, C. T., Nagy, A. F., Toth, G., Luhmann, J. G., et al. (2014). Effects of crustal field rotation on the solar wind plasma interaction with Mars. *Geophysical Research Letters*, *41*, 6563–6569. https://doi.org/10.1002/2014GL060785

Ma, Y., Nagy, A. F., Sokolov, I. V., & Hansen, K. C. (2004). Three-dimensional, multispecies, high spatial resolution MHD studies of the solar wind interaction with Mars. *Journal of Geophysical Research*, *109*, A07211. https://doi.org/10.1029/2003JA010367

Ma, Y., Russell, C., Fang, X., Dong, Y., Nagy, A. F., Toth, G., et al. (2015). MHD model results of solar wind interaction with Mars and comparison with MAVEN plasma observations. *Geophysical Research Letters*, *42*, 9113–9120. https://doi.org/10.1002/2015GL065218

Ma, Y., Russell, C. T., Nagy, A. F., Toth, G., Dong, C., & Bougher, S. W. (2013). Multi-fluid MHD study of the solar wind induced plasma escape from the Martian atmosphere. Abstract P13C-05 Presented at the 2013 AGU Fall Meeting, San Francisco, CA.

Ma, Y. J., Russell, C. T., Fang, X., Dong, C. F., Nagy, A. F., Toth, G., et al. (2017). Variations of the Martian plasma environment during the ICME passage on 8 March 2015: A time-dependent MHD, study. *Journal of Geophysical Research: Space Physics*, *122*, 1714–1730. https://doi.org/10.1002/2016JA023402

Ma, Y. J., Russell, C. T., Nagy, A. F., Toth, G., Dougherty, M. K., Wellbrock, A., et al. (2011). The importance of thermal electron heating in Titan's ionosphere: Comparison with Cassini T34 flyby. *Journal of Geophysical Research*, *116*, a10213. https://doi.org/10.1029/2011JA016657

Mahaffy, P. R., Benna, M., King, T., Harpold, D. N., Arvey, R., Barciniak, M., et al. (2015). The neutral gas and ion mass spectrometer on the Mars Atmosphere and Volatile Evolution Mission. *Space Science Reviews*, *195*, 49–73. https://doi.org/10.1007/s11214-014-0091-1

McFadden, J. P., Kortmann, O., Curtis, D., Dalton, G., Johnson, G., Abiad, R., et al. (2015). MAVEN SupraThermal and Thermal Ion Compostion (STATIC) instrument. *Space Science Reviews*, *195*, 199–256. https://doi.org/10.1007/s11214-015-0175-6

Mitchell, D. L., Mazelle, C., Sauvaud, J.-A., Thocaven, J.-J., Rouzaud, J., Fedorov, A., et al. (2016). The MAVEN solar wind electron analyzer. *Space Science Reviews*, *200*, 495–528. https://doi.org/10.1007/s11214-015-0232-1

Modolo, R., Chanteur, G. M., Dubinin, E., & Matthews, A. P. (2005). Influence of the solar EUV flux on the Martian plasma environment. *Annales Geophysicae*, *23*, 433–444. https://doi.org/10.5194/angeo-23-433-2005

Modolo, R., Chanteur, G. M., Dubinin, E., & Matthews, A. P. (2006). Simulated solar wind plasma interaction with the Martian exosphere: Influence of the solar EUV flux on the bow shock and the magnetic pile-up boundary. *Annales Geophysicae*, *24*(12), 3403–3410. https://doi.org/10.5194/angeo-24-3403-2006

Modolo, R., Hess, S., Mancini, M., Leblanc, F., Chaufray, J.-Y., Brain, D., et al. (2016). Mars-solar wind interaction: Lathys, an improved parallel 3-D multispecies hybrid model. *Journal of Geophysical Research: Space Physics*, *121*, 6378–6399. https://doi.org/10.1002/2015JA022324

Nagy, A. F., Winterhalter, D., Sauer, K., Cravens, T. E., Brecht, S., Mazelle, C., et al. (2004). The plasma environment of Mars. *Space Science Reviews*, *111*, 33–114. https://doi.org/10.1023/B:SPAC.0000032718.47512.92

Najib, D., Nagy, A. F., Tóth, G., & Ma, Y. (2011). Three-dimensional, multifluid, high spatial resolution MHD model studies of the solar wind interaction with Mars. *Journal of Geophysical Research*, *116*, A05204. https://doi.org/10.1029/2010JA016272

Ramstad, R., Barabash, S., Futaana, Y., Nilsson, H., & Holmström, M. (2016). Effects of the crustal magnetic fields on the Martian atmospheric ion escape rate. *Geophysical Research Letters*, *43*, 10,574–10,579. https://doi.org/10.1002/2016GL070135

Ramstad, R., Barabash, S., Futaana, Y., Nilsson, H., Wang, X.-D., & Holmström, M. (2015). The Martian atmospheric ion escape rate dependence on solar wind and solar EUV conditions: 1. Seven years of Mars Express observations. *Journal of Geophysical Research: Planets*, *120*, 1298–1309. https://doi.org/10.1002/2015JE004816

Richards, P. G., Fennelly, J. A., & Torr, D. G. (1994). EUVAC: A solar EUV flux model for aeronomic calculations. *Journal of Geophysical Research*, *99*(A5), 8981–8992. https://doi.org/10.1029/94JA00518

Schunk, R., & Nagy, A. (2000). *Ionospheres: Physics, plasma physics and chemistry*. Cambridge Atmospheric and Space Science Series: Cambridge University Press.

Simon, S., Boesswetter, A., Bagdonat, T., & Motschmann, U. (2007). Physics of the ion composition boundary: A comparative 3-D hybrid simulation study of Mars and Titan. *Annales Geophysicae*, *25*, 99–115. https://doi.org/10.5194/angeo-25-99-2007

Spreiter, J., Summers, A., & Rizzi, A. (1970). Solar wind flow past nonmagnetic planets—Venus and Mars. *Planetary and Space Science*, *18*, 1281–1299.

Terada, N., Shinagawa, H., Tanaka, T., Murawski, K., & Terada, K. (2009). A three-dimensional, multispecies, comprehensive MHD model of the solar wind interaction with the planet Venus. *Journal of Geophysical Research*, *114*, a09208. https://doi.org/10.1029/2008JA013937

Trotignon, J. G., Mazelle, C., Bertucci, C., & Acuña, M. H. (2006). Martian shock and magnetic pile-up boundary positions and shapes determined from the Phobos 2 and Mars global surveyor data sets. *Planetary and Space Science*, *54*, 357–369. https://doi.org/10.1016/j.pss.2006.01.003

Wang, X.-D., Alho, M., Jarvinen, R., Kallio, E., Barabash, S., & Futaana, Y. (2016). Emission of hydrogen energetic neutral atoms from the Martian subsolar magnetosheath. *Journal of Geophysical Research: Space Physics*, *121*, 190–204. https://doi.org/10.1002/2015JA021653

Wang, X.-D., Barabash, S., Futaana, Y., Grigoriev, A., & Wurz, P. (2014). Influence of Martian crustal magnetic anomalies on the emission of energetic neutral hydrogen atoms. *Journal of Geophysical Research: Space Physics*, *119*, 8600–8609. https://doi.org/10.1002/2014JA020307